



# Constructing ternary CdS/reduced graphene oxide/TiO<sub>2</sub> nanotube arrays hybrids for enhanced visible-light-driven photoelectrochemical and photocatalytic activity

Hui Li, Zhengbin Xia\*, Jiangqiong Chen, Liang Lei, Junheng Xing

School of Chemistry and Chemical Engineering, South China University of Technology, Guangzhou, Guangdong 510641, China

## ARTICLE INFO

### Article history:

Received 10 October 2014

Received in revised form 2 December 2014

Accepted 7 December 2014

Available online 24 December 2014

### Keywords:

TiO<sub>2</sub> nanotube arrays

Graphene

CdS

Ternary

Photocatalyst

## ABSTRACT

Ternary nanocomposite photoelectrodes composed of CdS nanocrystallites, reduced graphene oxide (RGO) and TiO<sub>2</sub> nanotube arrays (TNTs) are prepared by a coupling technique of electrophoretic deposition (EPD) and successive ionic layer adsorption and reaction (SILAR). Compare to pure TNTs, RGO/TNTs, and CdS/TNTs, the ternary CdS/RGO/TNTs hybrids show much higher visible-light-driven photoelectrochemical (PEC) and photocatalytic (PC) activity due to that the outer layer of CdS acts as sensitizer for trapping substantial photons from the visible light, the middle layer of RGO not only serves as electrons mediator and transporter for suppressing the recombination of photogenerated carriers, but also plays as a green sensitizer for enhancing visible light absorption, and the inner TNTs with narrowed band gap collect the hot electrons from the CdS and RGO to participate subsequent redox reaction for hydrogen production and organic pollutants degradation.

© 2014 Elsevier B.V. All rights reserved.

## 1. Introduction

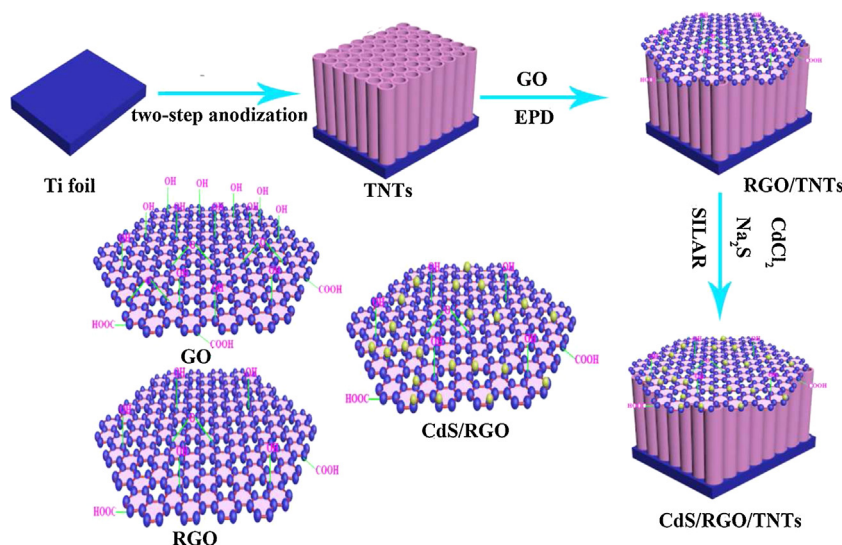
The conversion of solar energy to chemical energy using semiconductor photocatalysts has attracted increasing attention due to that it is one promising way to solve the energy crisis and environmental pollution problems. Semiconductor materials can act as the photocatalysts for light-induced chemical transformation, thanks to their unique electronic structure composed of a filled valence band (VB) and an empty conduction band (CB). Among all of the semiconductors, TiO<sub>2</sub> has been extensively and completely studied and used as photocatalysts because of its wonderful photocatalytic (PC) activity, high thermal and chemical stability, non-toxicity, and low-cost [1,2]. Unfortunately, the photoresponse of TiO<sub>2</sub> is confined to the UV light region which only accounts for less than 5% of the solar spectrum and the high recombination of the unstable photo-generated electron–hole pairs, thus restricting the PC activity and prospect of TiO<sub>2</sub>. In these regards, extending absorption region and boosting separation of photoexcited carriers are the two effective ways to enhance the PC activity of TiO<sub>2</sub>.

In recent years, one-dimensional (1-D) TiO<sub>2</sub> nanostructures have gained considerable attention owing to their alluring potential applications in diverse fields [3–5]. Compared to the bulk partic-

ulate TiO<sub>2</sub>, the 1-D TiO<sub>2</sub> nanostructures (nanowires, nanotubes and nanobelts) possess high aspect ratio, larger surface area, and provide a direct pathway for photogenerated electrons separation and transfer [6–8]. Among copious 1-D TiO<sub>2</sub> nanostructures, TiO<sub>2</sub> nanotube arrays (TNTs) prepared by electrochemical anodization of Ti foil have been demonstrated to be a extremely fascinating 1-D semiconductor materials which show excellent specific light absorption and propagation due to the well-defined nanotubular architecture and superb electric conductivity of the backside Ti substrate which further facilitate separation and transfer of photogenerated electron–hole pairs [9–12]. Thus, it is highly desirable to design 1-D anodized TNTs-based composite for promising applications in heterogeneous photocatalysis.

Recently, coupling of the anodized TNTs with narrow band gap semiconductors, such as CdS [13–16], CdSe [17–19], and PbS [20–22], have been utilized to improve the photoresponse of TNTs in the visible light region. Under visible light irradiation, these narrow band gap semiconductors can act as sensitizers and facilitate the photoexcited electrons flow from their CB to the CB of TNTs due to that the CB of these semiconductors is higher than that of TNTs, therefore assisting charge separation and improving visible-light-driven PC activity of the TNTs based nanocomposites. Among the different narrow band gap semiconductors, CdS can be easily prepared, and possesses suitable band gap (2.4 eV) and relatively high absorption coefficient in the visible light region, thus making it highly desirable for using as photocatalysts. However, for

\* Corresponding author. Tel.: +86 2087112047.  
E-mail address: [cezhbxia@scut.edu.cn](mailto:cezhbxia@scut.edu.cn) (Z. Xia).



**Scheme 1.** Schematic diagram of the ternary CdS/RGO/TNTs hybrids fabricated via a coupling technique of EPD and SILAR methods.

the CdS sensitized TNTs hybrids (CdS/TNTs), the sensitizer of CdS suffers from relatively low separation efficiency of electron–hole pairs and photocorrosion during light illumination, thus leading to energy loss, and instability of the hybrids [23,24]. Hence, a suitable medium is highly demanded to incorporate into the binary CdS/TNTs for overcoming their shortcomings.

Graphene, a two-dimensional honeycomb-like network of carbon atoms, has been widely used for preparing nanohybrids with semiconductors [25–29]. Various physico-chemical properties of the graphene shown in the graphene based photocatalysts indicate that the promising graphene can tackle the above mentioned bottlenecks of the binary CdS/TNTs junctions. The main reasons are shown as follows: (1) graphene is widely recognized as a perfect electron mediator and transporter to efficiently suppress recombination of photoexcited carriers, leading to high PC activity [30–32]. (2) For the hybrids of graphene and  $\text{TiO}_2$ , which show a red shift of the band edge and a great reduction of the band gap, which may be caused by the interaction between unpaired  $\pi$  electrons of graphene and Ti atoms or the chemical bonding between  $\text{TiO}_2$  and graphene [33]. (3) Graphene is an emerging type of photosensitizers in the binary  $\text{TiO}_2$  based hybrids, increasing the light absorption intensity for more efficient utilization of solar energy [34–37]. (4) The large surface area of graphene can provide plenty of surface active sites and increase the absorption of reactants [38,39]. (5) The deposited graphene films like a blanket may offer a protection to the CdS nanoparticles from photocorrosion [40]. With these regards, graphene is highly expected to be introduced into the binary CdS/TNTs for further enhancement of their PC activity and simultaneously increase the stability of CdS/TNTs system. Although several literatures have reported that the ternary CdS/RGO/ $\text{TiO}_2$ , the photoconversion efficiency is still unsatisfactory due to that the severe charge recombination occurs in the film of  $\text{TiO}_2$  particles; therefore, it is highly in demand to search new  $\text{TiO}_2$  morphology and structure to improve the charge separation and transfer [41,42]. However, to the best of our knowledge, few reports focus on incorporating graphene into the binary CdS/TNTs hybrids and understanding the function of graphene in the ternary nanocomposites.

Electrophoretic deposition (EPD) is one of the colloidal processes in nanomaterials fabrication and possesses merits of short formation time, simple apparatus, little restriction of the shape of substrate, and easy control of the thickness and morphology of deposited film [43,44]. Recently, Liu et al. fabricated RGO films

decorated TNTs (RGO/TNTs) through EPD of negative aqueous GO on the TNTs anode [40]. In addition, many previous literatures have reported that the successive ionic layer adsorption and reaction (SILAR) was a facial and effective method to deposit CdS nanoparticles on the TNTs [16,45–47]. Thus, we synthesized the ternary CdS-reduced graphene oxide- $\text{TiO}_2$  nanotube arrays hybrids (CdS/RGO/TNTs) via combining EPD and SILAR methods. As shown in Scheme 1, firstly, the highly ordered TNTs prepared by two-step anodization method which avoids formation of disordered and bundled arrays. Then the graphene oxide (GO) is electrophoretically (cyclic voltammetric mode) deposited on the TNTs to form the reduced graphene oxide modified TNTs nanocomposites (RGO/TNTs). Finally, the CdS nanoparticles are coupled on the RGO/TNTs by the SILAR technique (successive immersion of RGO/TNTs sample in solution of  $\text{Cd}^{2+}$  and  $\text{S}^{2-}$  to deposit CdS nanocrystallites on the RGO/TNTs surface). The CdS/RGO/TNTs photoelectrodes are characterized by SEM, TEM, FTIR, XPS, XRD, Raman, DRS and FL. Compare to the pristine TNTs, binary RGO/TNTs, and CdS/TNTs, the ternary CdS/RGO/TNTs hybrids exhibit much higher photoelectrochemical (PEC) and PC performance under visible light irradiation.

## 2. Experimental

### 2.1. Preparation of CdS/RGO/TNTs

Highly ordered TNTs were prepared by two-step anodization method similar to previous report [48]. Briefly, a two-electrode electrochemical cell, with a working electrode of Ti foil and a counter electrode of Pt foil, was used for the preparation of  $\text{TiO}_2$  nanotube arrays (TNTs). The titanium foils (purity 99.6%, thickness 1.0 mm) were firstly anodized in ethylene glycol (EG) electrolyte containing 0.5 wt%  $\text{NH}_4\text{F}$  and 2 vol% deionized water under 60 V for 2 h. Then the as-prepared  $\text{TiO}_2$  layer was peeled off by ultrasonication in deionized water. Subsequently, the well-patterned titanium foils were subjected to a second anodization in the EG electrolyte containing 0.5 wt%  $\text{NH}_4\text{F}$ , 0.5 wt%  $\text{H}_3\text{PO}_4$ , and 2 vol% deionized water at 60 V for 1 h. Finally, the as-anodized TNTs were annealed at 450 °C for 2 h.

Graphite oxide was synthesized using Hummers method by reacting the purified graphite powder (4 g,  $\leq 30 \mu\text{m}$ ) with a mixture of  $\text{H}_2\text{SO}_4$  (200 mL),  $\text{NaNO}_3$  (4 g), and  $\text{KMnO}_4$  (24 g) followed by the addition of  $\text{H}_2\text{O}_2$  (80 mL, 30%) [49]. The solid product was filtered

and washed repeatedly with deionized (DI) water and centrifugation, then dried under a vacuum at 50 °C. The obtained graphite oxide powder was exfoliated in DI water by ultrasonication for 45 min to form a homogeneous brown GO dispersion with a concentration of 0.5 mg/mL. The electrophoretic (CVs mode) reduction and deposition are performed with a two-electrode system (the annealed TNTs foil as working electrode, Pt foil as counter electrode) in the GO dispersion with slightly magnetic stirring. The CVs was conducted from  $-1.5$  to  $1$  V at a scan rate of  $50$  mV/s for 15 cycles. After deposition, the working electrode was washed with DI water and dried at room temperature. The SILAR process was performed to deposit the CdS crystallites on the RGO/TNTs to form the ternary CdS/RGO/TNTs hybrids. The RGO/TNTs electrodes immersed in a solution of  $0.1$  M  $\text{CdCl}_2$  for 5 min, they were then rinsed with DI water and immersed in a  $0.1$  M  $\text{Na}_2\text{S}$  solution for another 5 min followed by another rinsing with DI water. This SILAR process was repeated for 3 cycles.

## 2.2. Characterization

The morphologies of the samples were characterized by field-emission scanning electron microscopy (FE-SEM) (Nova NanoSEM 430, Holland) at an acceleration voltage of  $15$  kV. The transmission electron microscopy (TEM) (Hitachi H-7650, Japan) was used to observe the morphology details of individual tube of CdS/RGO/TNTs. Fourier transform infrared (FTIR) spectra were recorded using FTIR (PerkinElmer, 2200) spectrophotometer. X-ray photoelectron spectrometry (XPS, Kratos Axis Ultra DLD, UK) was used to detect the chemical composition of the as-prepared samples. The spectral positions were corrected by normalizing the C 1s spectrum at  $284.6$  eV, and a Shirley background was used for the peak fitting. X-ray diffraction (XRD) patterns were obtained on an X-ray diffractometer (Bruker D8 ADVANCE, Germany) using Cu K $\alpha$  radiation and operating at  $40$  kV/ $40$  mA. The Raman spectra were recorded by a LabRAM Aramis (Horiba Jobin Yvon, France) instrument, which was performed with the incidence power of  $10.4$  mW and the excitation wavelength of  $532$  nm. The UV–vis light absorption spectra were obtained from a Hitachi UV-3010 spectrophotometer (Japan) equipped with an integrating sphere assembly and using  $\text{BaSO}_4$  as a reference to measure all the samples. Fluorescence (FL) spectra were obtained using a fluorescence spectrometer (Hitachi F-7000). The excitation wavelength was  $280$  nm, with a scanning speed of  $600$  nm/min. The widths of the excitation slit and emission slit were  $2.5$  and  $5.0$  nm, respectively.

## 2.3. Photoelectrochemical (PEC) measurement

Photoelectrochemical measurements were carried out in  $1$  M KOH electrolyte with a standard three-electrode cell of the obtained sample, platinum foil and Ag/AgCl as the working, counter and reference electrode, respectively. The samples were illuminated by the filtered light ( $\lambda > 400$  nm,  $100$  mW/cm $^2$ ) provided by a PLS-SXE300UV Xe lamp (Changtuo, China). The intensity of the light source was measured using a radiant power meter (Instruments of Beijing Normal University) and the visible light was obtained using a UV-400 optical filter. The photocurrent response under zero bias was recorded with an Agilent digital multimeter. All experiments were carried out under ambient conditions. The electrochemical spectra (EIS) were performed on CHI660C under visible light illumination ( $100$  mW/cm $^2$ ) at open circuit voltage over a frequency range from  $10^5$  to  $0.1$  Hz with an AC voltage at  $10$  mV.

## 2.4. Photocatalytic (PC) test

The photocatalytic activity was measured in a XPA II reactor (Nanjing Xujiang Machineelectronic Plant, china). The samples

( $13 \times 10$  mm) were immersed in  $15$  mL quartz test tubes containing  $5$  mL methylene blue (MB,  $10$  mg/L) in the dark for  $30$  min to achieve adsorption equilibrium before radiation. After that, a  $1000$  W Xe lamp (the UV light was cut off by  $2.0$  M sodium nitrite) was used as the visible light source to conduct the photocatalytic experiment. The remaining MB concentration in the reaction solution was determined using the UV-2450 spectrophotometer (Japan).

The formation of hydroxyl radicals ( $\cdot\text{OH}$ ) at the photoilluminated samples/water interface can be detected by the fluorescence (FL) method using terephthalic acid as a molecule probe. Terephthalic acid can quickly react with  $\cdot\text{OH}$  to generate 2-hydroxyterephthalic acid, whose fluorescence intensity is proportional to the amount of  $\cdot\text{OH}$  generated in water. Experimental steps are similar to the measurement of PC except that MB aqueous solution is replaced by the  $5 \times 10^{-4}$  M terephthalic acid and  $2 \times 10^{-3}$  M NaOH. After photoreaction of  $30$  min, the fluorescence spectra of the resultant solution were measured on a Hitachi F-7000 fluorescence spectrophotometer. The employed excitation light for recording fluorescence spectra was  $320$  nm.

## 3. Results and discussion

### 3.1. Morphology and structure of CdS/RGO/TNTs hybrids

The scanning electron microscopy (SEM) images of the bare TNTs, RGO/TNTs, CdS/TNTs, and CdS/RGO/TNTs are shown in Fig. 1. The bare TNTs have a high-density, well-ordered, and uniform-arranged tubular structure with an average internal pore diameter of  $120$  nm and a length of about  $8.5$   $\mu\text{m}$  (Fig. 1(a)). After EPD (CVs mode) of GO on the TNTs, a continuous and transparent RGO film is formed on the top surface of TNTs (Fig. 1(b)). Then the RGO/TNTs are decorated with CdS by SILAR method, the nanocrystallites with average size of  $25$  nm are randomly distributed in the thin and flexible RGO film (Fig. 1(d)). While for the CdS/TNTs, the CdS nanocrystallites with uniform size of about  $10$  nm are uniformly decorated with the inner tube mouth (Fig. 1(c)). Energy dispersive X-ray analyser (EDX) fitted to the SEM chamber was used for determining the composition of the CdS/RGO/TNTs. The EDX spectrum (Fig. 1(e)) shows that the CdS/RGO/TNTs contain the elements of C, O, S, Ti and Cd, and the contents (wt% and at%) listed in the inset. The atom ratio of Cd and S is  $1.0068$ , which is proximal to  $1$ , in accordance with the intrinsic molar component of CdS. Transmission electronic microscopy (TEM) was explored to further confirm the presence of CdS and RGO in the TNTs. Fig. 1(f) shows the TEM image of individual nanotube of the CdS/RGO/TNTs obtained after ultrasonication. The RGO flakes are attached on the inner tube wall and the substantial CdS nanocrystallites are filled in the tube, which may be the result of ultrasonic process for obtaining individual nanotube.

Fourier transform infrared (FTIR) spectra were employed to characterize the carbon species in the prepared samples. Fig. 2(A) shows the FTIR spectra of GO, TNTs and CdS/RGO/TNTs. The GO exhibits absorption peaks corresponding to the stretching of  $-\text{OH}$  group (about  $3300$  cm $^{-1}$ ),  $\text{C}=\text{O}$  groups in carbonyl and carboxyl moieties ( $1726$  cm $^{-1}$ ),  $\text{C}=\text{C}$  skeletal vibration bands ( $1620$  cm $^{-1}$ ), epoxide  $\text{C}-\text{O}-\text{C}$  stretching vibration ( $1220$  cm $^{-1}$ ), and  $\text{C}-\text{O}$  stretching vibrations in epoxy or alkoxy groups ( $1045$  cm $^{-1}$ ) [50,51]. For the CdS/RGO/TNTs, all these main peaks are retained, but with a significant decrease in the peak intensity due to either the relatively low quantity of the deposited GO or the partial reduction of GO. To compare the change of GO functional groups between before and after electrochemical deposition process, X-ray photoelectron spectrometry (XPS) C 1s spectra of the prepared GO and CdS/RGO/TNTs are displayed in Fig. 2(B). For the GO, four peaks at  $284.5$ ,  $286.7$ ,  $287.5$ , and  $288.9$  eV, corresponding to  $\text{C}-\text{C}$ ,  $\text{C}-\text{O}$  in



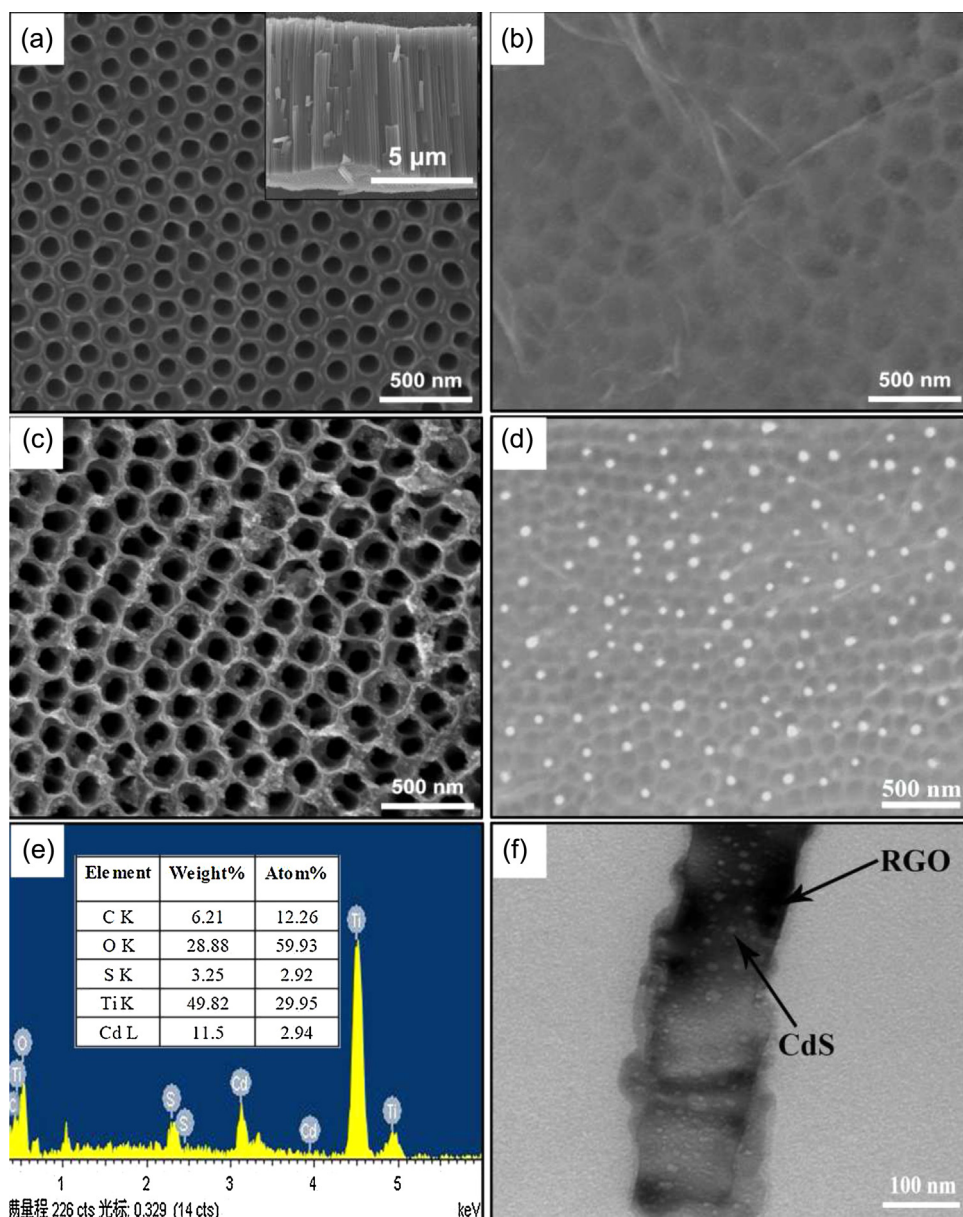


**Fig. 1.** Top-view SEM images of (a) pure TNTs, (b) RGO/TNTs, (c) CdS/TNTs, and (d) CdS/RGO/TNTs. (e) EDX spectrum and (f) TEM image of individual tube of CdS/RGO/TNTs. The inset in (a) is corresponding cross-sectional SEM image.

hydroxyl or epoxy groups, C=O, and O—C=O, respectively [52,53]. While for the CdS/RGO/TNTs, the peak intensity of C—O and C=O are obviously lower than the GO, and that of C—C and O—C=O are unchanged, which is attributed to that the electric field of EPD process leads to the GO is partial reduced to be RGO, and the O—C=O is often hard reduced. Moreover, the XPS C 1s spectra of the RGO and RGO/TNTs are displayed in Fig. S2. For the RGO which is slightly peeled from the RGO/TNTs, three peaks located at 284.5, 286.5 and 288.8 eV, correspond to C—C, C—O and O—C—O, respectively. For the intact RGO/TNTs, a new peak appears at 282.0 eV, which is attributed to O—Ti—C indicating the carbon atoms actually substitute the oxygen atoms of TiO<sub>2</sub> [54]. While no such peak arises in CdS/RGO/TNTs (Fig. 2(B)), which may be ascribed to that the top CdS layers hinder the precise detection of O—Ti—C in the TNTs.

X-ray diffraction (XRD) was employed to characterize the crystal phase of the ternary CdS/RGO/TNTs hybrids. As shown in Fig. 3(A), all the diffraction peaks can be well indexed to the anatase phase of TiO<sub>2</sub> (JCPDS No: 71-1167, marked by A) and Ti metal phase

(JCPDS No: 05-0682, marked by Ti). These peaks are originated from the TNTs and Ti substrate, respectively. Moreover, compared to the peaks of the annealed pure TNTs, there are three additional peaks at about 26.42°, 30.50°, and 43.12°, which are ascribed to (1 1 1), (2 0 0), (2 2 0) of the cubic structure of CdS (JCPDS NO: 77-2306, marked by C), respectively, and these peaks reveal that the CdS nanocrystallites are actually deposited on the CdS/RGO/TNTs hybrids. However, there is no indication of a graphene peak in the XRD patterns of CdS/RGO/TNTs, which may be due to the thin graphene layers that are below the detection limit of the XRD instrument [55]. Raman spectroscopy was adopted to further confirm the existence of RGO and CdS on the CdS/RGO/TNTs hybrids. Fig. 3(B) shows the peaks located at about 148, 397, 516 and 635 cm<sup>-1</sup>, which are corresponding to E<sub>g</sub>, B<sub>1g</sub>, B<sub>1g</sub> or A<sub>1g</sub>, E<sub>g</sub> modes of anatase phase [56]. The two peaks centered at about 1350 and 1595 cm<sup>-1</sup> are thought to be the characteristic D band and G band of the deposited RGO, respectively [30,57]. Moreover, it is worth noting that the peaks located at roughly 302 and 900 cm<sup>-1</sup> are

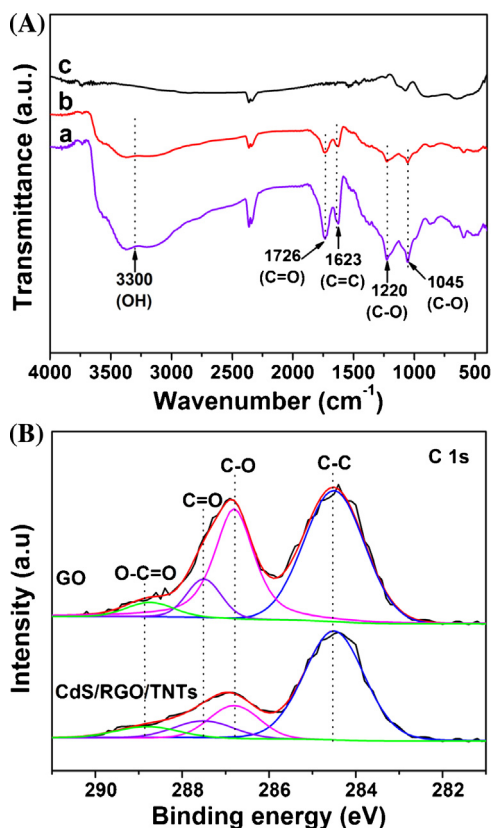


**Fig. 2.** (A) FTIR spectra of (a) GO, (b) CdS/RGO/TNTs, and (c) pure TNTs. (B) C 1s XPS spectra of GO and CdS/RGO/TNTs.

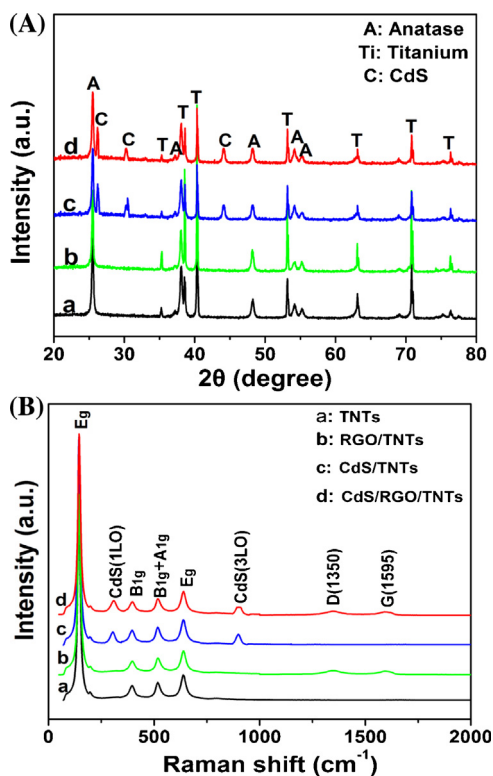


**Fig. 3.** (A) XRD patterns and (B) Raman spectra of (a) annealed pure TNTs, (b) RGO/TNTs, (c) CdS/TNTs, and (d) CdS/RGO/TNTs.

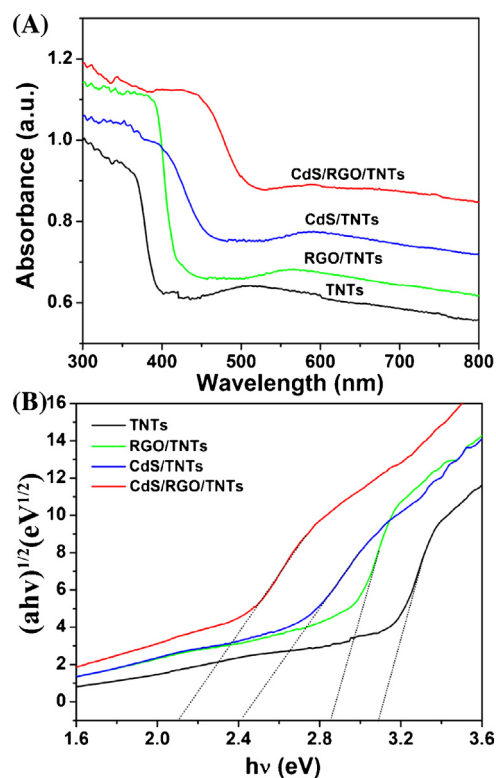


**Fig. 4.** (A) UV-vis diffuse reflectance spectra (DRS) of the TNTs, RGO/TNTs, CdS/TNTs, and CdS/RGO/TNTs. (B) Tauc plots which present variation of  $(\alpha h\nu)^{1/2}$  vs excitation energy ( $h\nu$ ) for the obtained samples to identify their band gaps.

ascribed to the optical phonon band 1LO and 3LO of CdS, respectively. However, the phonon band 2LO (about 600 cm<sup>-1</sup>) of CdS cannot be seen, which may be due to that the  $E_g$  (635 cm<sup>-1</sup>) region of anatase phase disguises the 2LO area of CdS [58,59]. The results from SEM, FTIR, XPS, XRD and Raman sufficiently confirm the formation of a sandwich-like structure of CdS/RGO/TNTs by EPD and SILAR methods.

### 3.2. Optical properties

The UV-vis diffuse reflectance spectra (DRS) of pure TNTs, RGO/TNTs, CdS/TNTs and CdS/RGO/TNTs are shown in Fig. 4(A). The RGO/TNTs and CdS/TNTs all show higher intensity than the pure TNTs in the visible light range, which is ascribed to that the RGO and CdS act as sensitizers for trapping a large number of visible light photons. The absorption intensity of CdS/RGO/TNTs is about 1.5 times that of pure TNTs due to the synergetic absorption effect of RGO and CdS. Moreover, an obvious red shift of the absorption edge from about 400 nm to 590 nm for the CdS/RGO/TNTs compared with the pure TNTs. Generally, optical transitions for crystalline semiconductors can be deduced from the variation of the absorption coefficient near the band edge. The optical absorption near the band edge is given by the following equation [60]:

$$\alpha = \frac{A(h\nu - E_g)^n}{h\nu} \quad (1)$$

where  $A$  is a constant,  $h$  is Planck's constant,  $\nu$  is the frequency and  $n$  denotes the transition mode. Due to the present anatase TNTs based composite is a type of indirect transition semiconductor, so the  $n=2$  in the Eq. (1) and we take value of 1 for the  $A$ . Then we convert the Eq. (1) into following form:

$$(\alpha h\nu)^{\frac{1}{2}} = h\nu - E_g \quad (2)$$

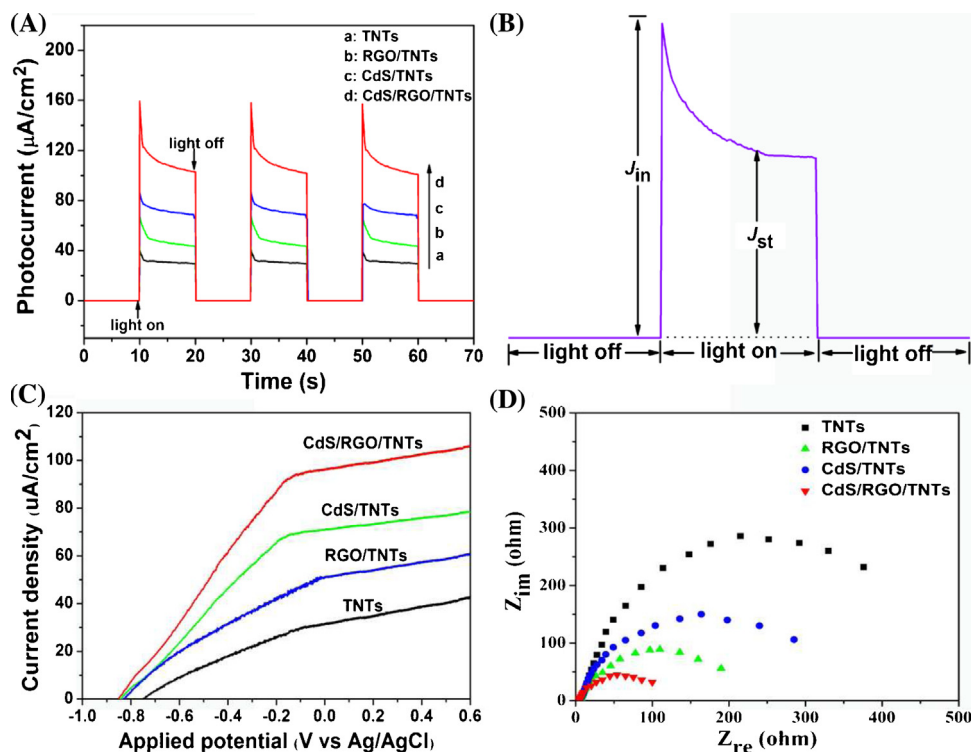


**Fig. 5.** (A) The transient photocurrent density of photoanodes including TNTs, CdS/TNTs, RGO/TNTs, and CdS/RGO/TNTs. (B) Schematic profiles of an ideal photocurrent response. (C) Linear-sweep voltammograms with scanning rate of 5 mV/s. (D) Electrochemical impedance spectra of Nyquist plots.

so the band gap ( $E_g$ ) can be obtained from the Tauc plot by extending a line from the maximum slope of the curve to the X-axis. Fig. 4(B) shows Tauc plots corresponding to each spectrum, which indicates that the band gap of pure anatase TNTs is 3.1 eV, approximate to the reported  $E_g$  value for anatase  $\text{TiO}_2$ . While the band gap of CdS/RGO/TNTs is significantly reduced to 2.1 eV. This phenomenon may be due to the sensitization of coupled CdS nanoparticles and the chemical bonding between C (partially derive from the RGO) and Ti during EPD process (Fig. S2). The significant enhanced ability of the CdS/RGO/TNTs photoelectrode to absorb visible light makes it a promising photocatalyst for solar-driven applications.

### 3.3. Photoelectrochemical and photocatalytic performance

To test PEC response of the prepared samples under visible light, photocurrent densities measured in the light on/off cycles under the bias of 0 V vs. Ag/AgCl are shown in Fig. 5(A). The photocurrent densities of CdS/RGO/TNTs, CdS/TNTs, and RGO/TNTs are about 105, 74, and 52  $\mu\text{A}/\text{cm}^2$ , respectively, 3.0, 2.1, and 1.5 times larger than that of the pure TNTs (35  $\mu\text{A}/\text{cm}^2$ ). Obviously, the photocurrent density of CdS/RGO/TNTs is about 200% higher than that of TNTs, that increment exceeds the sum of the increment with alone modification of CdS (111.4%) and RGO (48.6%), which sufficiently indicates there is synergistic effect in the ternary CdS/RGO/TNTs hybrids to improve their PEC performance. The results indicate that not only CdS but also RGO can capture the photons and suppress the recombination of the electron–hole pairs, and the ternary CdS/RGO/TNTs hybrids show more effective charge separation due to the simultaneous electron transfer from the CdS and RGO to the TNTs. In addition, the CdS/RGO/TNTs exhibit ideal photocurrent density transient profiles (Fig. 5(B)). Upon visible light illumination, the photoanode of CdS/RGO/TNTs show relatively large photocurrent density tip ( $J_{in}$ ) due to that the sudden photogenerated separation of electron–hole pairs. Then the tip gradually decays

as the carriers migrate from the inside of hybrids to the surface and some of the electron–hole pairs recombine within the hybrids. A steady state photocurrent density ( $J_{st}$ ) is subsequently achieved since the equilibrium between the electron diffusion rate and its generation rate, and electrons continuously collected in backside Ti substrate for hydrogen production and holes accumulated at the interface of electrolyte to oxidize water to form OH radicals. Finally, the separated carriers rapidly recombine in dark and show no photocurrent density. In addition, the photo-corrosion of CdS nanoparticles under light irradiation is key problem and also a challenge for their photoelectrochemical applications. To investigate this issue in our present ternary system, we conducted the amperometric  $I-t$  measurements under simulated solar light illumination with 60 s light on–off cycle for 2 h (Fig. S1). The photocurrent density decay rates of CdS/TNTs and CdS/RGO/TNTs are 14.7% and 6.8%, respectively. This difference may be attributed to two aspects, the one is that light absorption effect of RGO layers which has been shown in Fig. 4(A) and the other one is that parts of CdS nanoparticles deposited on the concave area of RGO layers because the deposited RGO layers on the surface of TNTs is crinkled rather than flat, just like a blanket which has been reported by the previous literature [40]. Therefore minimized photo-corrosion effects are shown in the present ternary composite. Linear-sweep voltammograms of different prepared electrodes are shown in Fig. 5(C). Upon visible light illumination, the current gradually increases with increasing applied potential from  $-1$  to  $0 \text{ V}_{\text{Ag/AgCl}}$ , indicating photogenerated hole–electron pairs separation resulting from the electric field. At higher potential ( $E > 0 \text{ V}_{\text{Ag/AgCl}}$ ), a saturation of the photocurrent is observed for all samples, which can be attributed to the field distribution on the nanotubes. In addition, the onset potentials of CdS/TNTs, RGO/TNTs, and CdS/RGO/TNTs all shift negatively compared with that of pristine TNTs (from  $-0.85 \text{ V}_{\text{Ag/AgCl}}$  to  $-0.75 \text{ V}_{\text{Ag/AgCl}}$ ). The shift of the onset potential might be due to a lower band bending requirement for separating electrons and holes because of better charge-transport properties for the coupled TNTs



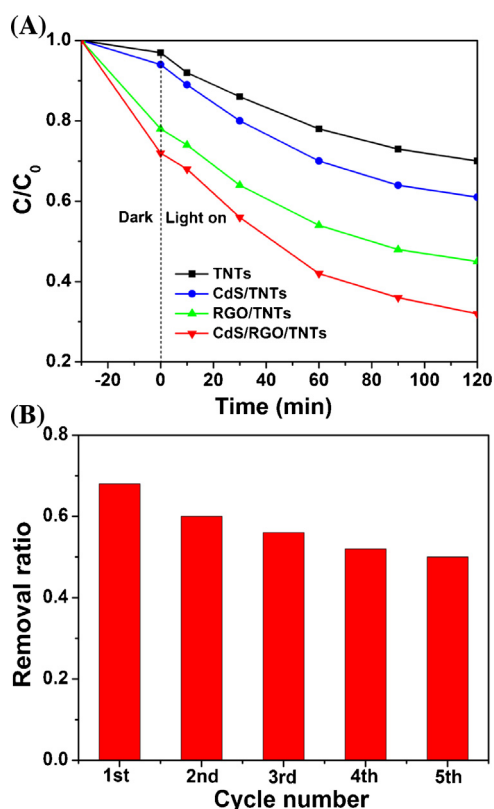


**Fig. 6.** (A) Visible-light-driven photocatalytic degradation rates of MB over pure TNTs, CdS/TNTs, RGO/TNTs, and CdS/RGO/TNTs. (B) Recycled photocatalytic decomposition of MB for CdS/RGO/TNTs.

than pure TNTs. Electrochemical impedance spectra (EIS) provides a powerful method to study the charge transfer and recombination processes at semiconductor-electrolyte interface and the diameter of the semicircle in the Nyquist plot is equal to the charge transfer resistance ( $R_{ct}$ ). A typical Nyquist plot obtained in 1 M KOH aqueous solution under visible light illumination for the prepare samples is shown in Fig. 5(D). Both CdS/RGO/TNTs and RGO/TNTs hybrids show lower  $R_{ct}$  than CdS/TNTs and bare TNTs, which may be attributed to the introduction of the conductive RGO layer. It should be noted that the CdS/RGO/TNTs show smallest  $R_{ct}$  value,

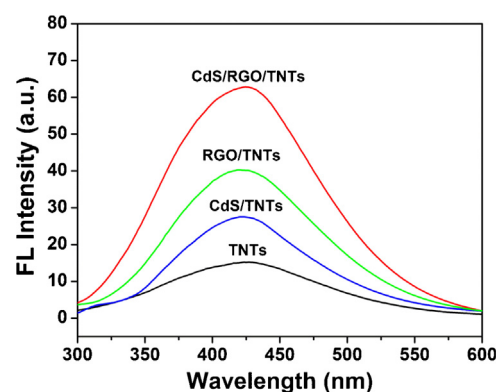


**Fig. 7.** Fluorescence (FL) signal spectra of formed 2-hydroxyterephthalic acid over pure TNTs, CdS/TNTs, RGO/TNTs, and CdS/RGO/TNTs after visible light irradiation for 30 min.

indicating the charge transfer is further enhanced by placing the RGO layer between CdS and TNTs.

The PC activity of the prepared TNTs, RGO/TNTs, CdS/TNTs, and CdS/RGO/TNTs were evaluated by the degradation of methylene blue (MB) under visible light illumination as shown in Fig. 6(A). Before irradiation, 30 min adsorption in the dark was applied to ensure sufficient adsorption of MB on the prepared photocatalysts. Obviously, both CdS/RGO/TNTs and RGO/TNTs show higher adsorption capacity than the pristine TNTs and CdS/TNTs, which is attributed to the strong  $\pi$ - $\pi$  conjugated connections between the benzene rings and the surface of RGO [61]. After 120 min visible light irradiation, the CdS/RGO/TNTs photocatalyst shows a MB removal efficiency of about 70%, much higher than 55% over RGO/TNTs, 39% over CdS/RGO, and 30% over pure TNTs. By comparison, the RGO/TNTs exhibit better PC performance than the pure TNTs, which presumably benefits from the high charge separation, transfer, and adsorptive capacity of RGO. Moreover, it is clearly seen that the ternary CdS/RGO/TNTs hybrids show decomposition efficiency much larger than the binary CdS/TNTs and RGO/TNTs composites, indicative of a synergetic effect between CdS nanoparticles and RGO. Fig. 6(B) shows the PC stability of CdS/RGO/TNTs hybrids. Apparently, their PC activity is deteriorated after five consecutive PC experiments. It can be speculated that the absorbed MB molecules tightly integrate with the RGO through chemisorptions, and they are not easily washed away when the photocatalyst is

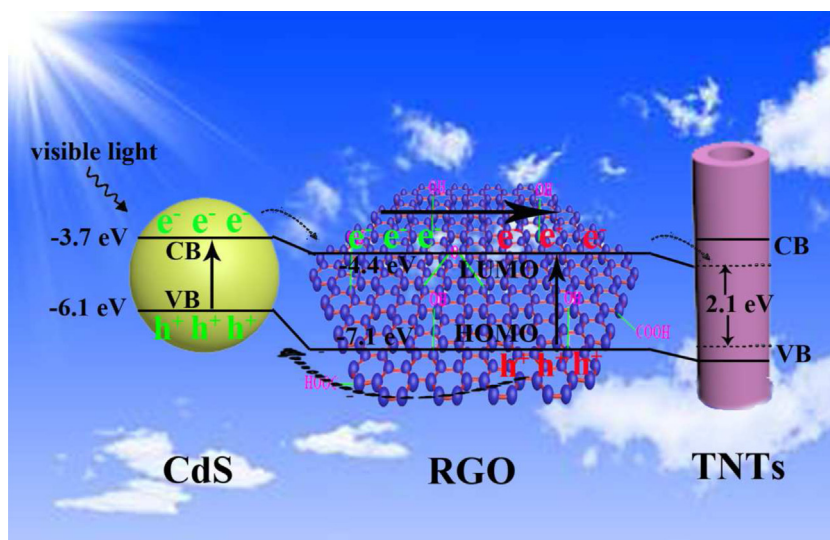


**Fig. 8.** Schematic diagram of the interfacial photogenerated charge carriers separation and transfer within the photoelectrode of ternary CdS/RGO/TNTs hybrids.

regenerated for the next recycle, resulting in reducing the adsorption capacity toward fresh MB solution and decreasing the PC efficiency during the same reaction period. These results sufficiently demonstrate that the ternary CdS/RGO/TNTs hybrids have high PC activity and good stability, thus can be applied as a superb photocatalyst for degrading organic pollutants.

To illustrate the relationship between the carriers separation and PC properties in the prepared samples, a terephthalic acid (TA) fluorescence probe was used to detect hydroxyl radicals ( $\bullet$ OH) generated in the reaction system under visible light irradiation. Terephthalic acid (TA) can quickly reacts with  $\bullet$ OH to generate 2-hydroxyterephthalic acid, whose fluorescence intensity is proportional to the amount of  $\bullet$ OH [62,63]. As shown in Fig. 7, the FL intensity shows a gradually decrease from the CdS/RGO/TNTs, RGO/TNTs, CdS/TNTs to pure TNTs, meaning the generated amount of  $\bullet$ OH decrease in the same order. This result may be due to the lowest degree of charge recombination and the longest lifetimes of the carriers in the ternary composite system.

Fig. 8 schematically shows the proposed mechanism for the charge carriers separation and transfer within the photoelectrode of ternary CdS/RGO/TNTs hybrids. Under visible light irradiation, for the outer sensitizer layer of CdS, the electrons on its valence band (VB) ( $-6.1$  eV) are excited to conduction band (CB) ( $-3.7$  eV) due to the unique electronic structure ( $E_g = 2.4$  eV) of semiconductor. Then the excited electrons flow to the LUMO orbit of RGO through overcoming the Schottky barrier between CdS and RGO since the energy level of RGO ( $-4.4$  eV) is lower than the CB of CdS. Simultaneously, the electrons on the HOMO of RGO are also stimulated to its LUMO because of the photosensitizer role of graphene, which has been demonstrated by various reports [34–37]. All the excited electrons stored on the LUMO of RGO are subsequently injected to the CB of the modified TNTs whose band gap is sufficiently narrowed ( $3.2$ – $2.1$  eV) as the interaction between unpaired  $\pi$  electrons of graphene and Ti atoms or the chemical bonding between  $\text{TiO}_2$  and graphene [64,65]. For the PC degradation of MB process, the excited electrons are easily trapped by the absorbed MB molecules on the TNTs surface producing superoxide anion radicals ( $\bullet\text{O}_2^-$ ) which are powerful oxidizing agents for decomposing dye molecules. Besides, for the PEC water splitting process, the excited electrons on the CB of TNTs rapidly migrate to the backside conductive Ti foil and continuously flow to the counter Pt electrode for hydrogen production through the external circuit. As a result, the separated electrons and holes can be fully involved in PEC and PC reactions, and a highly corresponding activity is achieved.

#### 4. Conclusions

In this study, the ternary CdS/RGO/TNTs hybrids are prepared via a combining technique of EPD and SILAR methods. The hydrophilic RGO nanosheets deposited onto the surface of TNTs, and the CdS nanocrystallites randomly distributed on the RGO films. FTIR and XPS results sufficiently demonstrate that the reactant of GO is reduced to RGO by the EPD process. XRD and Raman characterization works confirm the CdS and RGO are successfully coupled with the TNTs. The ternary CdS/RGO/TNTs hybrids exhibit much higher visible-light-driven PEC response and PC degradation activity than the pure TNTs and binary TNTs based composite (CdS/TNTs and RGO/TNTs). A possible explanation is the different roles of each component in the ternary hybrids, namely the outer sensitizer layer of CdS is responsible for absorbing substantial photons from visible light, the middle layer of RGO not only act as electrons reservoirs and transmitter for facilitating excited electron–hole pairs but also serve as a green photosensitizer for further increasing photons capture, and the supporting base of TNTs play the role of superb electrons acceptor for redox reactions. Thus, it presents a new

insight on the designation and construction of multiple TNTs-based nanohybrids for efficient visible-light-driven photocatalysts.

#### Acknowledgement

This work was supported by the National Natural Science Foundation of China (NSFC, NO. 20976058).

#### Appendix A. Supplementary data

Supplementary data associated with this article can be found, in the online version, at <http://dx.doi.org/10.1016/j.apcatb.2014.12.029>.

#### References

- [1] S.-C. Moon, H. Mametsuka, S. Tabata, E. Suzuki, *Catal. Today* 58 (2000) 125–132.
- [2] J. Du, X. Lai, N. Yang, J. Zhai, D. Kisailus, F. Su, D. Wang, L. Jiang, *ACS Nano* 5 (2010) 590–596.
- [3] Y. Xia, P. Yang, Y. Sun, Y. Wu, B. Mayers, B. Gates, Y. Yin, F. Kim, H. Yan, *Adv. Mater.* 15 (2003) 353–389.
- [4] L. Zhang, J.C. Yu, M. Mo, L. Wu, K.W. Kwong, Q. Li, *Small* 1 (2005) 349–354.
- [5] Y. Zhang, Z.-R. Tang, X. Fu, Y.-J. Xu, *ACS Nano* 5 (2011) 7426–7435.
- [6] S.P. Albu, A. Ghicov, J.M. Macak, R. Hahn, P. Schmuki, *Nano Lett.* 7 (2007) 1286–1289.
- [7] X. Feng, K. Shankar, O.K. Varghese, M. Paulose, T.J. Latempa, C.A. Grimes, *Nano Lett.* 8 (2008) 3781–3786.
- [8] T. Tachikawa, T. Majima, *J. Am. Chem. Soc.* 131 (2009) 8485–8495.
- [9] K. Zhu, N.R. Neale, A. Miedaner, A.J. Frank, *Nano Lett.* 7 (2007) 69–74.
- [10] K.G. Ong, O.K. Varghese, G.K. Mor, K. Shankar, C.A. Grimes, *Sol. Energy Mater. Sol. Cells* 91 (2007) 250–257.
- [11] J.R. Jennings, A. Ghicov, L.M. Peter, P. Schmuki, A.B. Walker, *J. Am. Chem. Soc.* 130 (2008) 13364–13372.
- [12] K. Shankar, J.I. Basham, N.K. Allam, O.K. Varghese, G.K. Mor, X. Feng, M. Paulose, J.A. Seabold, K.-S. Choi, C.A. Grimes, *J. Phys. Chem. C* 113 (2009) 6327–6359.
- [13] S. Chen, M. Paulose, C. Ruan, G.K. Mor, O.K. Varghese, D. Kouzoudis, C.A. Grimes, *J. Photochem. Photobiol. A* 177 (2006) 177–184.
- [14] W.-T. Sun, Y. Yu, H.-Y. Pan, X.-F. Gao, Q. Chen, L.M. Peng, *J. Am. Chem. Soc.* 130 (2008) 1124–1125.
- [15] S. Banerjee, S.K. Mohapatra, P.P. Das, M. Misra, *Chem. Mater.* 20 (2008) 6784–6791.
- [16] D.R. Baker, P.V. Kamat, *Adv. Funct. Mater.* 19 (2009) 805–811.
- [17] A. Kongkanand, K. Tvrđy, K. Takechi, M. Kuno, P.V. Kamat, *J. Am. Chem. Soc.* 130 (2008) 4007–4015.
- [18] Y. Liang, B. Kong, A. Zhu, Z. Wang, Y. Tian, *Chem. Commun.* 48 (2012) 245–247.
- [19] H. Yang, W. Fan, A. Vaneski, A.S. Susha, W.Y. Teoh, A.L. Rogach, *Adv. Funct. Mater.* 22 (2012) 2821–2829.
- [20] C. Ratanatawanate, C. Xiong, K.J. Balkus Jr., *ACS Nano* 2 (2008) 1682–1688.
- [21] C. Ratanatawanate, Y. Tao, K.J. Balkus Jr., *J. Phys. Chem. C* 113 (2009) 10755–10760.
- [22] Q. Kang, S. Liu, L. Yang, Q. Cai, C.A. Grimes, *ACS Appl. Mater. Interfaces* 3 (2011) 746–749.
- [23] A.P. Davis, C. Huang, *Water Res.* 25 (1991) 1273–1278.
- [24] D. Fermin, E. Ponomarev, L. Peter, *J. Electroanal. Chem.* 473 (1999) 192–203.
- [25] G. Williams, B. Seger, P.V. Kamat, *ACS Nano* 2 (2008) 1487–1491.
- [26] A. Cao, Z. Liu, S. Chu, M. Wu, Z. Ye, Z. Cai, Y. Chang, S. Wang, Q. Gong, Y. Liu, *Adv. Mater.* 22 (2010) 103–106.
- [27] I.V. Lightcap, T.H. Kosel, P.V. Kamat, *Nano Lett.* 10 (2010) 577–583.
- [28] Y.H. Ng, A. Iwase, A. Kudo, R. Amal, *J. Phys. Chem. Lett.* 1 (2010) 2607–2612.
- [29] Y.T. Liang, B.K. Vijayan, K.A. Gray, M.C. Hersam, *Nano Lett.* 11 (2011) 2865–2870.
- [30] C. Chen, W. Cai, M. Long, B. Zhou, Y. Wu, D. Wu, Y. Feng, *ACS Nano* 4 (2010) 6425–6432.
- [31] N.J. Bell, Y.H. Ng, A. Du, H. Coster, S.C. Smith, R. Amal, *J. Phys. Chem. C* 115 (2011) 6004–6009.
- [32] L. Gu, J. Wang, H. Cheng, Y. Zhao, L. Liu, X. Han, *ACS Appl. Mater. Interfaces* 5 (2013) 3085–3093.
- [33] J.S. Lee, K.H. You, C.B. Park, *Adv. Mater.* 24 (2012) 1084–1088.
- [34] Y. Zhang, N. Zhang, Z.R. Tang, Y.J. Xu, *ACS Nano* 6 (2012) 9777–9789.
- [35] M.Q. Yang, Y.J. Xu, *J. Phys. Chem. C* 117 (2013) 21724–21734.
- [36] C.H. Kim, B.H. Kim, K.S. Yang, *Carbon* 50 (2012) 2472–2481.
- [37] P. Song, X. Zhang, M. Sun, X. Cui, Y. Lin, *Nanoscale* 4 (2012) 1800–1804.
- [38] Y. Wen, H. Ding, Y. Shan, *Nanoscale* 3 (2011) 4411–4417.
- [39] L.C. Sim, K.H. Leong, S. Ibrahim, S. Pichiah, *J. Mater. Chem. A* 2 (2014) 5315–5322.
- [40] C. Liu, Y. Teng, R. Liu, S. Luo, Y. Tang, L. Chen, Q. Cai, *Carbon* 49 (2011) 5312–5320.
- [41] N. Zhang, Y. Zhang, X. Pan, M. Yang, Y. Xu, *J. Phys. Chem. C* 116 (2012) 18023–18031.



- [42] C.Y. Park, U. Kefayat, N. Vikram, T. Ghosh, W.C. Oh, K.Y. Cho, *Bull. Mater. Sci.* 36 (2013) 869–876.
- [43] L. Besra, M.A. Liu, *Prog. Mater. Sci.* 52 (2007) 1–61.
- [44] A. Chavez-Valdez, M. Shaffer, A. Boccaccini, *J. Phys. Chem. B* 117 (2012) 1502–1515.
- [45] S. Cheng, W. Fu, H. Yang, L. Zhang, J. Ma, H. Zhao, M. Sun, L. Yang, *J. Phys. Chem. C* 116 (2012) 2615–2621.
- [46] Y. Lai, Z. Lin, D. Zheng, L. Chi, R. Du, C. Lin, *Electrochim. Acta* 79 (2012) 175–181.
- [47] D. Zhang, J. Zhang, Q. Wu, X. Miao, *J. Am. Ceram. Soc.* 93 (2010) 3284–3290.
- [48] Z. Zhang, P. Wang, *Energy Environ. Sci.* 5 (2012) 6506–6512.
- [49] W.S. Hummers Jr., R.E. Offeman, *J. Am. Chem. Soc.* 80 (1958) 1339.
- [50] Y. Xu, H. Bai, G. Lu, C. Li, G. Shi, *J. Am. Chem. Soc.* 130 (2008) 5856–5857.
- [51] H.L. Guo, X.F. Wang, Q.Y. Qian, F.B. Wang, X.H. Xia, *ACS Nano* 3 (2009) 2653–2659.
- [52] J. Zhang, Z. Xiong, X. Zhao, *J. Mater. Chem.* 21 (2011) 3634–3640.
- [53] X. Wei, C.M. Chen, S. Guo, F. Guo, X. Li, X. Wang, H. Cuiht, L. Zhao, W. Li, *J. Mater. Chem. A* 2 (2014) 4667–4675.
- [54] H. Wang, Z. Wu, Y. Liu, *J. Phys. Chem. C* 113 (2009) 13317–13324.
- [55] Y. Hu, L. Lu, J. Liu, W. Chen, *J. Mater. Chem.* 22 (2012) 11994–12000.
- [56] G. Tian, H. Fu, L. Jing, B. Xin, K. Pan, *J. Phys. Chem. C* 112 (2008) 3083–3089.
- [57] K.N. Kudin, B. Ozbas, H.C. Schniepp, R.K. Prud'Homme, I.A. Aksay, R. Car, *Nano Lett.* 8 (2008) 36–41.
- [58] J.S. Suh, J.S. Lee, *Chem. Phys. Lett.* 281 (1997) 384–388.
- [59] M.L. Curri, A. Agostiano, L. Manna, M.D. Monica, M. Catalano, L. Chiavarone, V. Spagnolo, M. Lugarà, *J. Phys. Chem. B* 104 (2000) 8391–8397.
- [60] M.A. Batler, *J. Appl. Phys.* 48 (1977) 1914–1920.
- [61] T. Wu, X. Cai, S. Tan, H. Li, J. Liu, W. Yang, *Chem. Eng. J.* 173 (2011) 144–149.
- [62] Q. Xiao, Z. Si, J. Zhang, C. Xiao, X. Tan, *J. Hazard. Mater.* 150 (2008) 62–67.
- [63] J. Yu, W. Wang, B. Cheng, B.L. Su, *J. Phys. Chem. C* 113 (2009) 6743–6750.
- [64] C. Nethravathi, M. Rajamathi, *Carbon* 46 (2008) 1994–1998.
- [65] H. Zhang, X. Lv, Y. Li, Y. Wang, J. Li, *ACS Nano* 4 (2009) 380–386.